A Nonparametric Temperature Controller With Nonlinear Negative Reaction for Multi-Point Rapid MR-Guided HIFU Ablation

Lorena Petrusca*, Vincent Auboiroux, Thomas Goget, Magalie Viallon, Arnaud Muller, Patrick Gross, Christoph D. Becker, and Rares Salomir

Abstract—**Magnetic resonance-guided high intensity focused ultrasound (MRgHIFU) is a noninvasive method for thermal ablation, which exploits the capabilities of magnetic resonance imaging (MRI) for excellent visualization of the target and for near real-time thermometry. Oncological quality of ablation may be obtained by volumetric sonication under automatic feedback control of the temperature. For this purpose, a new nonparametric (i.e., model independent) temperature controller, using nonlinear negative reaction, was designed and evaluated for the iterated sonication of a prescribed pattern of foci. The main objective was to achieve the same thermal history at each sonication point during volumetric MRgHIFU. Differently sized linear and circular trajectories were investigated *ex vivo* and *in vivo* using a phased-array HIFU transducer. A clinical 3T MRI scanner was used and the temperature elevation was measured in five slices simultaneously with a voxel size of $1 \times 1 \times 5$ mm^3 and temporal resolution of 4 s. *In vivo* results indicated a similar thermal history of each sonicated focus along the prescribed pattern, that was $17.3 \pm 0.5\ °C$ as compared to $16\ °C$ prescribed temperature elevation. The spatio-temporal control of the temperature also enabled meaningful comparison of various sonication patterns in terms of dosimetry and near-field safety. The thermal build-up tended to drift downwards in the HIFU transducer with a circular scan.**

Index Terms—**High intensity focused ultrasound (HIFU), magnetic resonance (MR) thermometry, nonparametric temperature controller, volumetric sonication.**

I. INTRODUCTION

MAGNETIC resonance-guided high intensity focused ultrasound (MRgHIFU) has a recognized potential for the minimally-invasive therapy of localized cancer. One major

*L. Petrusca is with Faculty of Medicine, University of Geneva, 1211 Geneva, Switzerland, and also with Hôpitaux Universitaires de Genève, Service de radiologie (P)-CIBM, CH-1211 Genève 14, Switzerland (e-mail: lorena.petrusca@unige.ch).

V. Auboiroux and T. Goget are with the Faculty of Medicine, University of Geneva, 1211 Geneva, Switzerland.

R. Salomir is with Faculty of Medicine, University of Geneva, 1211 Geneva, Switzerland, and also with the Radiology Department, University Hospitals of Geneva, 1211 Geneva, Switzerland.

M. Viallon and C. D. Becker are with the Radiology Department, University Hospitals of Geneva, 1211 Geneva, Switzerland.

A. Muller is with the Radiology Department, Lyon-Sud Hospital, University Hospitals of Lyon, 69495 Pierre-Bénite, France.

P. Gross is with Siemens HealthCare, Magnetic Resonance, 91052 Erlangen, Germany.

Color versions of one or more of the figures in this paper are available online at http://ieeexplore.ieee.org.

Digital Object Identifier 10.1109/TMI.2014.2310704

practical requirement is to achieve uniform thermal ablation, i.e., of oncological quality. The focal zone of the HIFU beam is millimeter-sized and, hence electronic or mechanical displacement of the focus is necessary to treat an entire tumor. Considering liver malignancies, for example, a total volume of 1–20 cc should be treated in one session [1]; this volume being 100–1000 times larger than the elementary focal lesion produced by a HIFU device. Moreover, ablation margins of 5–8 mm are required to reduce the risk of local recurrence.

The MRgHIFU technique performed by sequential elementary sonication (also known as the point-by-point ablation technique) has been investigated clinically to determine the technical feasibility [2]–[4]. However, an important amount of heat is lost with this approach due to the diffusion process around small ablated regions and thus, the total duration of the treatment is increased.

The volumetric sonication approach has significantly improved treatment efficiency and ablation homogeneity, by implementing the focus displacement along a predefined trajectory while continuously sonicating (i.e., duty-cycle near to 100%) [5]–[8]. The tissue's natural heat diffusion is employed to produce the fusion of each individual focus into macrolesions and to homogenize the thermal build-up, while the temperature elevation on the heated region's borders limits the cooling-down process of the central zone.

Detailed investigations of the region of interest, optimal planning of the therapy, and active control of the temperature elevation are required to obtain a safe and effective anti-cancer MRgHIFU thermotherapy. MR imaging is a noninvasive technique and offers essential advantages for the real-time guidance of guiding tools for ultrasound therapy [9], [10]. Detailed anatomical information and near real-time accurate temperature maps can be obtained using MRI; the preferred method of MR thermometry being the PRFS [11]–[13]. For a successful thermoablation, the accumulation of a lethal dose must be guaranteed in the tumor region, while in the surrounding healthy tissue, the dose should remain as low as possible. Online active feedback of the accumulated thermal dose in the region of interest remains a major issue in terms of clinical applicability. To ensure the delivery of an equivalent thermal dose at every sonicated point of the trajectory, and to control the HIFU exposure during heating, an accurate and robust temperature controller is required. Reproducible and predictable ablation volumes without *a priori* knowledge of tissue parameters are highly desirable [14].

Clinical studies using MRgHIFU indicated a large variability for uterine leiomyoma treatment, including over- and under-treatment of the region of interest due to the temperature dependence on unknown tissue-specific parameters [15]. Therefore, the need for spatio-temporal temperature control has been addressed with a variety of approaches in the past. The experimental implementation of automatic temperature control in MRgHIFU faces several difficulties. The first problem concerns the initial set of tuning parameters used for the controller's equation, which are dependent on a number of factors, such as the effective heat conduction, nonlinear blood perfusion, and linear or nonlinear ultrasound absorption, etc., [16]. A controller is also sensitive to MR thermometry parameters including spatial resolution, temporal sampling, volumetric coverage or noise standard deviation. In addition, different errors due to experimental noise can occur, and the thermal feedback loop must be robust against any external perturbation.

A temperature controller based on a proportional–integral–derivative (PID) algorithm was described in [17] for extracorporeal single focus HIFU, and later its stability and convergence were investigated *ex vivo* [16] for automatically MRI-controlled contact ultrasound thermal therapy. The algorithm was based on a multi-input/single-output static-tuning PID feedback loop. The controller's performance suggested that a tailor-made thermal model with two static parameters is appropriate for the MR-guided therapeutic ultrasound when the rate of heating is rather slow.

A homogenous temperature profile could be obtained by modulating the velocity of the HIFU transducer for volumetric ablations obtained mechanically [5], or by reoptimizing the heated points after each electronic trajectory [18], [19].

Chopra *et al.* [20] reported accurate active control of temperature during single sweeping for transurethral continuous ultrasound ablation. In that study, rotational motion of the transducer and thermal mapping were performed simultaneously. Relevant results were obtained by numerical simulations concerning the sensitivity of a temperature-based feedback algorithm to spatial and nonspatial parameters for transurethral ultrasound prostate treatment [21].

The purpose of the current study was to develop and to evaluate (*ex vivo* and *in vivo*) a new nonparametric (i.e., model independent) temperature controller using nonlinear negative reaction, dedicated to volumetric sonication with an iterated pattern of foci, aiming to deliver rapidly an equivalent thermal dose for each focus. In addition, various MRgHIFU sonication patterns (based on linear and circular trajectories) were performed *ex vivo* and *in vivo* and analyzed from the perspective of the thermal build-up drift towards the near field.

II. MATERIALS AND METHODS

A. Theory

1) Rapidly Convergent Multi-Input/Multi-Output Nonparametric Temperature Controller: To develop and implement the new temperature controller, different principles of treatment were determined.

a) A sonication cycle represents the sequential displacement of the focus through all prescribed foci.

b) The foci are successively sonicated by electronic steering, such that one sonication cycle is completed in the same duration as that of one measurement of temperature (or equivalent with the temporal resolution of MRT); therefore, the sampling time (or dwell time, denoted as τ) of the feedback loop is the same for each focus location and is set by the MRT

$$\tau = \text{sampling time} = \text{MRT temporal resolution}$$

.

c) The controller tries to compensate the local temperature deviation at each focus compared with the average temperature over all foci.

d) The controller updates the portion of energy to be delivered at each focus and cycle (product power × time per point).

e) The distance between foci must be larger than the intrinsic size of the focal spot (for individual identification), but not too large, to enable the formation of a continuous thermal build-up by exploiting heat diffusion; a 4-mm gap is suggested as optimal for a typical sonication time of 1 min and tissue diffusivity of 0.13 mm^2/s.

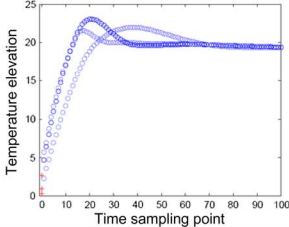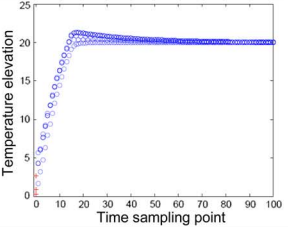f) The number of cycles is decided *a priori* or adjusted on-the-fly based on accumulated thermal dose.

2) Controller Modification Compared With the Initial PID. Description With Continuous Function Formalism, Parametric Implementation: Within the scope of the present paper, we are using the following symbols.

$\alpha(\vec{r}_o, t)$	Effective heat deposition rate at point $\vec{r}_o$ and time t due to the absorption of the ultrasound energy.
τ	Dwell time (temporal resolution of MR thermometry).
$\Theta(t)$	Prescribed (or target) evolution of the temperature.
D	Effective diffusion coefficient (also called diffusivity) in tissue, considered locally uniform and isotropic, also including the sink effect of the perfusion if any.
$T(\vec{r}_o, t)$	Experimental (measured) temperature at point $\vec{r}_o$ and time t.
$\Delta(\vec{r}_o, t) = \Theta(t) - T(\vec{r}_o, t)$	Current error at location $\vec{r}_o$.
$\Omega(\vec{r}_o, t) = \int_0^t [\Theta(t') - T(\vec{r}_o, t')] dt'$	Time integrated error at location $\vec{r}_o$.

Herein, we are presenting the principal modifications compared with the initial temperature controller at single focus of type PID, described in Salomir *et al.*, 2000. These modifications are further summarized in the Table I. When the spatio-temporal coordinates are not provided as arguments of variables, in order to simplify the mathematical expressions, the list above applies.

Let us consider a closed-loop feedback regulator, which is ideal in the sense that there is no temporal latency when applying the feedback command, while the input and output signals are noise-free. The well-known PID controller has

TABLE I

	PID algorithm (Salomir et al., 2000)	P^{2}ID algorithm (New algorithm)
Master equation for updating the applied energy	$E(\vec{r}_o,t) = \dfrac{\tau}{\alpha(\vec{r}_o)} \left\{ \begin{array}{l} \dfrac{d\Theta(t)}{dt} - D \cdot \nabla^2 T(\vec{r}_o,t) + \\ + q \cdot \Delta(\vec{r}_o,t) + \dfrac{q^2}{4} \cdot \Omega(\vec{r}_o,t) \end{array} \right\}$	$E(\vec{r}_o,t) = \dfrac{\tau}{\alpha(\vec{r}_o)} \left\{ \begin{array}{l} \dfrac{d\Theta(t)}{dt} - D \cdot \nabla^2 T(\vec{r}_o,t) + \\ + w \cdot t \cdot \Delta(\vec{r}_o,t) + w \cdot \Omega(\vec{r}_o,t) \end{array} \right\}$
Recommended values for negative reaction whilst noise-robust	$q \approx \dfrac{0.20}{\tau} \cdots \dfrac{0.25}{\tau}$	$w \approx \dfrac{0.20}{\tau^2} \cdots \dfrac{0.25}{\tau^2}$
Characteristic differential equation	$\dfrac{d^2\Omega}{dt^2} + q \cdot \dfrac{d\Omega}{dt} + \dfrac{q^2}{4} \cdot \Omega = 0$	$\dfrac{d^2\Omega}{dt^2} + w \cdot t \cdot \dfrac{d\Omega}{dt} + w \cdot \Omega = 0$
Time-domain convergent solution (TDCS)	$\Omega(t) \propto \left(1 - \dfrac{q \cdot t}{2}\right) \cdot exp\left(-\dfrac{q \cdot t}{2}\right)$	$\Omega(t) \propto exp\left(-\dfrac{w \cdot t^2}{2}\right)$
Numerical simulation of convergence when confronted with varying absorption coefficient of HIFU in tissue (33% to 300% of true value)		
Convergence time	$\dfrac{2}{q}$: typical 8…10 sampling points	$\sqrt{\dfrac{2}{w}}$: typical $\sqrt{8} \ldots \sqrt{10}$ sampling points
Interpretation	**P^{2}ID algorithm has 3-fold stronger convergence than PID algorithm under experimental constraints, typical for MRgHIFU**	

been used in the past for automatic temperature control during MR-guided focused ultrasound hyperthermia [16]–[18], [20], [22]. The thermal energy to be deposited by the acoustic wave at the focus during the dwell time τ is given by the following master equation:

$$E(\vec{r}_o,t) = \frac{\tau}{\alpha(\vec{r}_o)} \left\{ \frac{d\Theta(t)}{dt} - D \cdot \nabla^2 T(\vec{r}_o,t) + q \cdot \Delta(\vec{r}_o,t) \right.$$
$$\left. + \frac{q^2}{4} \cdot \Omega(\vec{r}_o,t) \right\}. \quad (1)$$

The parameter adjusting the negative reaction strength q has the dimension of s^{-1} and is inversely proportional to the convergence time of the controller

$$\tau_c = \frac{2}{q}. \quad (2)$$

A differential, integral or integral-differential associated equation of various orders, depending on the type of controller, can be then written in the time domain to describe the dynamic evolution of the error metrics between the actual state function and the prescribed one. The time-domain associated equation for the PID controller applied to thermal therapy is the condition that reduces expression (1) to the bioheat transfer equation. The time-domain associated equation for the PID controller is of the type of a second-order differential

$$\frac{d^2\Omega}{dt^2} + q \cdot \frac{d\Omega}{dt} + \frac{q^2}{4} \cdot \Omega = 0. \quad (3)$$

The solution of (3), determined up to constants related to the initial conditions, can be written as

$$\Omega(t) = (C_1 + C_2 \cdot t) \cdot exp\left(-\frac{q \cdot t}{2}\right). \quad (4)$$

The exponential convergence indicated by (4) was demonstrated to be experimentally sufficient for the automatic temperature control of single point HIFU sonication [17], slow mechanically swept HIFU volumetric ablation [18], and unfocussed sonication with contact applicator [20]. The rapid volumetric ablation based on phased array steering yields more severe constraints and therefore, is our goal in proposing a more powerful controller in terms of temporal convergence. In particular, we shall increase the polynomial order of the negative argument in the exponential operator, obtaining a Gaussian-like expression, determined up to a constant related to the initial conditions

$$\Omega(t) = C \cdot \exp\left(-\frac{w \cdot t^2}{2}\right). \quad (5)$$

Beyond the powerful convergence, expression (5) has the mathematical advantage of being the analytical solution of a linear second-order differential equation with nonconstant coefficients

$$\frac{d^2\Omega}{dt^2} + w \cdot t \cdot \frac{d\Omega}{dt} + w \cdot \Omega = 0. \quad (6)$$

The negative reaction parameter w has the dimension of s^{-2} and is inversely proportional to the squared convergence time of the controller

$$\tau_c = \sqrt{\frac{2}{w}}. \qquad (7)$$

Using the same inference as for the association of expressions (1) and (3), and by defining expression (6) to be the time-domain associated equation of a new feedback controller, this yields a P^2ID-type controller ruled by the following master equation:

$$E(\vec{r}_o, t) = \frac{\tau}{\alpha(\vec{r}_o)} \left\{ \frac{d\Theta(t)}{dt} - D \cdot \nabla^2 T(\vec{r}_o, t) + w \right.$$
$$\left. \cdot t \cdot \Delta(\vec{r}_o, t) + w \cdot \Omega(\vec{r}_o, t) \right\}. \quad (8)$$

Note, a higher order exponent in expression (5) (e.g., $t^3, t^4, \ldots$) may be chosen if required, but the feedback command would involve higher order time-dependent weights, too. Comparison of expressions (1) and (8) brings into focus the first important modification in the present work compared with past reports; the weight of the proportional term of the negative reaction is linearly increasing with time.

3) Controller Modification to Nonparametric and Discrete-Time Implementation: Further modification of the controller formalism is required to adapt it for multi-point volumetric sonication. Expression (8) significantly enhances the convergence over the previous PID-type of controller, but it still has several disadvantages.

- It includes tissue-dependent parameters (α, D) that in general are not accurately known.
- It is valid for one isolated focal point and does not take into account possible "cross talk" between foci, i.e., energy deposition at one location while sonicating another location, because the beam shape has a spatial profile that is different to a Dirac-type distribution.
- It is expressed with time-continuous functions while the experimental data are always sampled with discrete-time.

To take into account the specific nature of the multi-focus sonication, we need to define the actual error spatially as well as temporally. That is, the actual measured temperature at each focus is compared first to the spatial average over the set of foci at a given measurement time-point during the rising temperature regime, and second, it is compared with the prescribed (or target) value of temperature elevation (Θ_{top}) after the steady-state regime was reached. The regime is switched at sampling point n_{switch}. The rising regime ($1 \leq n \leq n_{switch}$) is defined by the aim to reach as fast as possible a target value of temperature elevation, and the steady-state regime ($n > n_{switch}$) is defined by the aim to maintain a constant (stable) temperature at each focus for a prescribed duration.

Comparing one individual focus temperature to the spatial average over other foci is equivalent to redefining the target temperature during the rising regime on-the-fly, according to

$$\Theta_n = \begin{cases} \frac{1}{N_f} \sum_{k=1}^{N_f} T_{k,n}, & \text{during rising regime } 1 \leq n \leq n_{switch} \\ \Theta_{top}, & \text{during steady} \\ & - \text{state regime } n > n_{switch} \end{cases}$$
$$(9)$$

where N_f is the total number of foci in the sonication pattern, $n = 1, 2, 3, \ldots$ is the MR thermometry scan temporal index, $k = 1, 2, \ldots N_f$ is the spatial index of each focus, and $T_{k,n}$ is the measured temperature at scan n and focus k.

Subsequently, the proportional and respectively, integral metrics of error in the spatio-temporal state function under the time-discrete formalism become

$$\Delta_{k,n} = 1 - \frac{T_{k,n}}{\Theta_n}$$
$$\Omega_{k,n} = \sum_{n'=1}^{n} \left(1 - \frac{T_{k,n'}}{\Theta_{n'}} \right). \qquad (10)$$

This is the second important modification of the implemented controller compared with past reports.

Furthermore, as a third important modification, we hypothesize that the improved power of convergence of the P^2ID controller is sufficient to allow accurate experimental performance, even when no physical parameter of the tissue is involved in the feedback command. In other words, it is sufficient to appropriately modulate the set of focus-specific delivered energy values, at each time point, in order to homogenize the measured temperatures over all foci without explicitly considering the local absorption of ultrasound, nor the local intensity of the beam steering-dependent and the local heat conductivity. The spatio-temporal modulation of the delivered energy at focus k and measurement n is expressed as

$$E_{k,n} = E_{k,1} \cdot (1 + F_{k,n}) \text{ with } n \geq 2 \qquad (11)$$

where $E_{k,1}$ is the initial set of values for the foci $k = 1, 2, \ldots, N_f$ and $F_{k,n}$ is the feedback command to the applied energy per dwell time. For circular scan sonication, the values of $E_{k,1}$ are constant for each focus, given the geometrical symmetry. Conversely, for line scan sonication, the values of $E_{k,1}$ are compensated *a priori* for focal energy loss with steering and for enhanced heat diffusion at the edges of the pattern [Fig. 1(a)]. The central issue is now defining the expression of $F_{k,n}$.

One important observation is that the information about average energy absorption and heat diffusion is implicitly contained in the time interval necessary for the controller to reach the steady-state regime, i.e., the elapse of time until sampling point n_{switch}. For instance, low absorption and high diffusion will tend to increase n_{switch}. Conversely, high absorption and low diffusion will tend to decrease n_{switch}. Another important observation is that the amount of energy necessary to maintain the steady state is also related to n_{switch}. If the steady state was reached rapidly, then little energy is required to maintain that temperature at the prescribed value. If n_{switch} tends to infinity, the steady state cannot be reached and the applied energy per dwell time is maintained equal to the initial (or maximum) value. These observations can be transposed mathematically by using a C_2-class mathematical function monotonously varying between 0 and 1, to relate n_{switch} to the amount of energy necessary to maintain the steady state (as a fraction of the initially set energy per dwell time); for instance, a hyperbolic tangent.
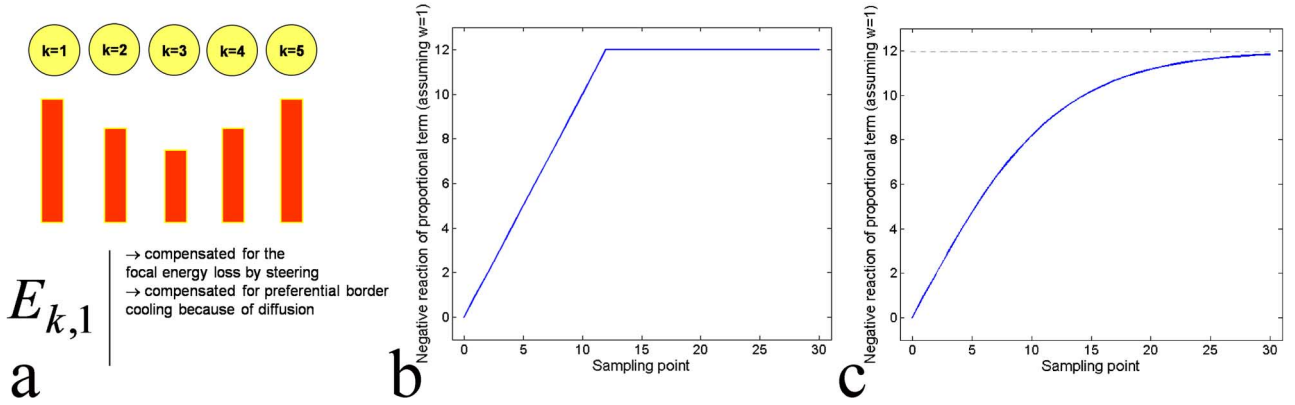
Fig. 1. (a) Example of 10 individual foci arranged in two parallel lines. Index k is referencing the focus 1:N_f. $E_{k,1}$ is the initial amount of energy prescribed for each focus ($scan = 1$), considering (*a priori*) the energy loss by steering and the preferential peripheral heat diffusion. During the procedure, $E_{k,1}$ would be modulated by the temperature controller to ensure similar temperature elevation at each focus. Threshold limitation (b) and hyperbolic tangent limitation (c) of the negative reaction of the proportional term in the controller's equation.

One more technical step is to define a nondimensional parameter that adjusts the negative reaction

$$w^* = w \cdot \tau^2. \tag{12}$$

Finally, the master equation of the time-discrete, nonparametric, nonlinear reaction controller is written as shown in (13) at the bottom of the page.

The weighting of n_{switch} by the factor of 2.5% in the hyperbolic tangent function was determined experimentally as a good compromise for various heating patterns and different types of tissue. Physically, this means that 2.5% of the initial energy is required to maintain steady-state condition hypothetically reached after a single dwell time interval of sonication.

Table II summarizes the main modifications required to implement the nonparametric controller. The energy delivered at each focus location is the meaningful physical action. The first choice for controlling this energy was to modulate the portion of time spent by the HIFU beam at each focus location, while always keeping invariant the duration of the sonication cycle, i.e., successive iterations over all foci. If the temporal modulation became incompatible with the condition of the fixed duration of the sonication cycle (summation of time portions too short or too long), the fixed duration condition still had priority. In that case, the energy balance between foci was achieved by changing the focus-wise power level while inversely proportionally changing the focus-wise time portions of sonication.

4) Criteria for Irreversible Switching to Steady-State Form of Master Equation: The controller algorithm decides when to switch to the steady-state computing equation, i.e., when the sampling point is declared equal to n_{switch}. This is done in a predictive way.

Sampling point "n" becomes "n_{switch}" if the following condition is fulfilled:

$$[\theta_n + (\theta_n - \theta_{n-1})] > (\theta_{\text{top}} - \delta). \tag{14}$$

Textually, this means that the predicted temperature elevation after one more sonication cycle will exceed the transition level. Here, $\delta = 0.5\,°C$. The predicted temperature elevation is the actual value plus the last increment between the previous and current cycle. The transition is decided irreversibly. Once the master equation was switched to the steady-state form, this one would be used until the end of the active heating.

5) Limiting the Negative Reaction of the Proportional Term: According to the equations provided above, the proportional term brings a negative reaction that increases linearly with time. Because the temperature data are contaminated by experimental noise, an overweighted negative reaction can drive the controller into instability.

Moreover, it is important that the negative reaction increases linearly during the "learning" stage, which corresponds to the time interval of the first 10–15 dynamics. Once the temperature has reached the steady-state level ("cruise altitude"), the heating device only needs to compensate for local cooling by diffusion and perfusion, and the negative reaction can be stabilized.
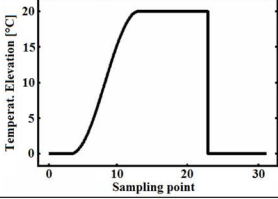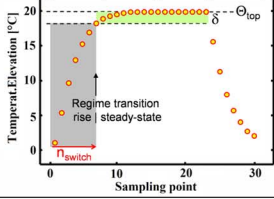
Therefore, we modified the master equation for the controller output by limiting the negative reaction of the proportional term using a modulation function $M(n)$, as shown in (15) at the bottom of the next page. Two variants of the modulation function are exemplified here [Fig. 1(b) and (c)]:

• threshold limitation: $M(n) = \min(n, n_{\text{max}})$
• hyperbolic tangent: $M(n) = n_{\text{max}} \cdot \tanh(n/n_{\text{max}})$

with recommended value n_{max} in the range of 10–20 (see Fig. 1(b) where $n_{\text{max}} = 12$), as evaluated from the requirement

$$F_{k,n+1} = \begin{cases} w^* \cdot n \cdot \left(1 - \dfrac{T_{k,n}}{\Theta_n}\right) + w^* \cdot \Omega_{k,n}, & \text{if } 1 \leq n \leq n_{switch} \\[2em] -1 + tahn(0.025 {*} n_{\text{switch}}) + w^* \cdot n \cdot \left(1 - \dfrac{T_{k,n}}{\Theta_{\text{top}}}\right) + w^* \cdot \Omega_{k,n}, & \text{if } n > n_{switch}. \end{cases} \tag{13}$$

TABLE II

	Parametric & continuous time description	Non-parametric & discrete-time implementation with adimensional numbers
Controlled variable	$T(\vec{r}_o,t)$	MR-measured temperature $T_{k,n}$: k = spatial index over foci $1{:}N_f$ n = MRT scan index
Objective function	$\Theta(t)$	Θ_n : n=1,2,3,… MRT scan index
Definition of objective function	Continuous and derivable scalar function (rising portion + flat-top region)	$\Theta_n = \begin{cases} \dfrac{1}{N_f}\sum\limits_{k=1}^{N_f} T_{k,n} & if \quad \Theta_n \leq \Theta_{top}-\delta \Leftrightarrow \mathrm{n} \leq \mathrm{n_{switch}} \\[2ex] \Theta_{top} & if \quad \Theta_n > \Theta_{top}-\delta \Leftrightarrow \mathrm{n} > \mathrm{n_{switch}} \end{cases}$
Graphical view of the objective function		
Current error	$\Delta(\vec{r}_o,t)=\Theta(t)-T(\vec{r}_o,t)$	$\Delta_{k,n}=1-\dfrac{T_{k,n}}{\Theta_n}$: relative error (focus k, scan n)
Integral error	$\Omega(\vec{r}_o,t)=\int\limits_0^t \left[\Theta(t')-T(\vec{r}_o,t')\right]dt'$	$\Omega_{k,n}=\sum\limits_{n'=1}^{n}\left(1-\dfrac{T_{k,n'}}{\Theta_{n'}}\right)$: cumulative relative error
Controller output	$E(\vec{r}_o,t)=\dfrac{\tau}{\alpha(\vec{r}_o)}\left\{\begin{array}{l}\dfrac{d\Theta(t)}{dt}+D\cdot\nabla^2 T(\vec{r}_o,t)+\\ +w\cdot t\cdot\Delta(\vec{r}_o,t)+w\cdot\Omega(\vec{r}_o,t)\end{array}\right\}$	$w^*=w\cdot\tau^2$ $E_{k,n}=E_{k,1}\cdot\left(1+F_{k,n}\right)$ with $\mathrm{n}\geq 2$ $F_{k,n+1}=\begin{cases} w^*\cdot n\cdot\left(1-\dfrac{T_{k,n}}{\Theta_n}\right)+w^*\cdot\Omega_{k,n} & if \quad \mathrm{n}\leq\mathrm{n_{switch}} \\[2ex] -1+\tanh(0.025*n_{switch})+w^*\cdot n\cdot\left(1-\dfrac{T_{k,n}}{\Theta_{top}}\right)+w^*\cdot\Omega_{k,n} & else \end{cases}$

of a rapid ablation and the typical sampling rate of the process (i.e., temporal resolution of MR thermometry). Overall, the present controller is based on a "universal" algorithm and thus, no tissue-specific parameter tuning is required.

B. Experimental Demonstration

1) Experimental Setup: The experiments were performed on a clinical whole-body MRI scanner (Magnetom Tim-Trio system, Siemens AG, Germany, maximum gradient $\mathrm{strength}=45\ \mathrm{mT/m}$ and maximum slew $\mathrm{rate}=200\ \mathrm{T/m/s}$) using a GRE-EPI sequence with echo train length 9, $\mathrm{TE}=8.9\ \mathrm{ms}$, $\mathrm{TR}=161\ \mathrm{ms}$, flipangle $=10°$, bandwidth $=500\ \mathrm{Hz/pixel}$, voxel $1\times1\times5\ \mathrm{mm}^3$, 40–60 dynamic scans. The intrinsic precision of the MR thermometry was calculated based on a dynamic acquisition of 30 measurements performed without HIFU sonication in a homogenous

region [23]. The average precision varied spatially following the sensitivity profile of the loop coil and ranged between 0.2°C to 0.4 °C *ex vivo* and between 0.4 °C and 0.6 °C *in vivo*. Five slices (1 axial + 1 sagittal each aligned with the HIFU beam main axis, and 3 coronal with 10-mm gap; temporal resolution: 4 s) were acquired interleaved using the high-resolution PRFS MRT method [12], [24]. In the current implementation, the controller software is fed with the temperature information from the central coronal slice. MR images were sent to an online display interface in real time, using a fast Ethernet connection. An MR-compatible phased array HIFU transducer (256 elements, F = 1030 kHz, spherical shape, radius 130 mm, aperture 140 mm, element diameter 6.6 mm, intrinsic focal spot size at −6 dB intensity $1\times1\times8\ \mathrm{mm}^3$, manufactured by Imasonic, Besançon, France) was used to produce sonications *ex vivo* in homogenous and heterogenous tissue models and *in vivo*

$$F_{k,n+1}=\begin{cases} w^*\cdot\mathrm{M}(n)\cdot\left(1-\dfrac{T_{k,n}}{\Theta_n}\right)+w^*\cdot\Omega_{k,n}, & if\ 1\leq n\leq n_{switch} \\[3ex] -1+\tanh(0.025*n_{switch})+w^*\cdot\mathrm{M}(n)\cdot\left(1-\dfrac{T_{k,n}}{\Theta_{\mathrm{top}}}\right)+w^*\cdot\Omega_{k,n}, & if\ n>n_{switch}. \end{cases}$$

(15)

in sheep thighs. A mechanical system was used for LR (left, right) and HF (head, feet) translations of the HIFU transducer, while the phased array was driven by a 256-channel generator (both from Image Guided Therapy, Pessac-Bordeaux, France), which provided an independent control of the signal frequency (range $= 0.5 - 10$ MHz), amplitude (accuracy $= 0.4\%$), and phase shift (accuracy $= \lambda/256$) for each element. The Ethernet communication with the beamformer to update the phase and amplitude for the 256 channels took less than 5 ms, and the focal point position could be changed electronically 20 times/s (Ox: 30 mm, Oz: 30 mm, and Oy: 50 mm around the natural focal point) in order to follow any complex trajectory. Maximum acoustic power used in this study was 300 W (pre-calibrated by acoustic balance measurements); the delivered power being monitored online during sonication for each channel. The MR host computer was equipped with real-time data export facilities via an Ethernet connection. Note that for all the described experiments, the HIFU transducer was placed horizontally in the MR magnet, and the symmetry axis of the HIFU beam was vertical within the magnet frame. An 11-cm surface loop coil (receive-only) was used with the HIFU beam propagating through the coil aperture. Software written in-house was used for online trajectory planning, HIFU monitoring, and hardware control.

For *ex vivo* experiments sampled consisted of either homogenous (Turkey pectoral muscle) or heterogenous (bovine kidney embedded in Turkey pectoral muscle) tissues, degassed for 30 min under vacuum, while *in vivo* experiments were conducted on six healthy sheep (mean weight $= 30$ kg) under general anesthesia without waking up, in the thigh muscle (single or both thighs). The *in vivo* protocol was approved by the Animal Research Ethics Committee of the University of Geneva and by the Cantonal Veterinary Authority of Geneva. The skin was carefully prepared to enable optimal propagation of HIFU. The animals were sacrificed immediately after the HIFU experiments by IV injection of KCl.

2) Sonication Patterns: Taking advantage of the flexible experimental setup and the "universal" P^2ID controller's formulation, different sonication trajectories were executed by fast electronic switching of focus position. In particular, linear and circular scan trajectories were applied in the treatment plane (orthogonal to the HIFU beam). Different segment lengths and circle diameters (8, 16, and 24 mm) were tested in independent *ex vivo* experiments, adjusting the total duration of sonication proportionally to the pattern size. For *in vivo* experiments, we performed 16-mm-sized linear trajectories (nine ablations) and circular trajectories (seven ablations). The foci positions along the entire sonication pattern were iteratively swept by the steered HIFU beam during each MR acquisition of one data volume (i.e., the number of iterative sonication cycles equal to the number of MR thermometry dynamic scans). Intra-cycle ordering of foci sonication was center-to-border for linear patterns and sequential along the circular perimeter. The duration of ablative sonication was prescribed according to the following equation:

$$\text{DURATION [sec]} = 7.5 \,[\text{sec/mm}] * \text{PATTERN}_{\text{SIZE}} \,[\text{mm}]$$

where PATTERN_SIZE stands for the length of the linear segment or for the diameter of the circle. The corresponding number

of MR thermometry dynamic measurements covering the ablative sonication was, respectively, 15, 30, and 45 for pattern sizes of 8, 16, and 24 mm, corresponding to time durations of 60, 120, and 180 s.

Prior to ablative sonication, *in situ* correction of the foci positions was applied. This consisted of a pilot sonication of 10 s active HIFU with acoustical power between 100 and 120 Wac, delivered to an under-sampled pattern as follows.

- Three collinear points [distant by half of the segment length, see Fig. 2(a)–(c) for linear sonication.
- Four points positioned symmetrically [one point per quadrant, see Fig. 2(d)–(f) for circular sonication.

Geometric correction of the effective foci coordinates was performed if misalignment was found in the pilot sonication, see Appendix for details. Then, the ablative HIFU sonication was performed, chained automatically 12 s after the end of the pilot sonication, during the same MR acquisition.

The acoustic energy at each individual focus was *a priori* time-compensated for the acoustic intensity loss during steering [see Fig. 1(a)] and further controlled by the closed feedback loop [see (11) and (15)]. The role of the automatic closed-loop control of energy deposition was to produce a similar temperature elevation at each location.

The duration of one sonication cycle was constant throughout the procedure and equal to the MRT temporal resolution. Each focal point in the sonication pattern was targeted sequentially and a portion of the sonication cycle time was assigned to that focal point. The intra-cycle relative distribution of time portions was modified by the controller. If the summation of calculated time portions exceeded the prescribed constant duration of one sonication cycle, all focus-wise time portions were multiplied by a sub-unitary factor and the applied power was multiplied by the inverse of that factor. The time portion per focus cannot be less than 50 ms (hardware limitation); in this case the applied power was reduced while maintaining the minimum sonication time of 50 ms. The target temperature elevation (i.e., relative temperature) tracked by the automatic controller was set at 17.5 °C for the *ex vivo* experiments and at 16 °C for the *in vivo* tests (corresponding to 54 °C absolute temperature for the *in vivo* experiments). Dosimetric data were calculated after treatment in order to characterize the efficacy of each sonicated pattern.

III. RESULTS

A. Ex Vivo Experimental Demonstration of the Temperature Controller

The temperature controller's *ex vivo* experimental demonstration showed excellent stability when performing different sonication patterns. Fig. 3 illustrates the temperature build-up in three orthogonal planes (a: axial, b: sagittal, and c, d: coronal) for three different linear MRgHIFU sonications ($L = 8$, $L = 16$, and $L = 24$ mm). A uniform thermal build-up can be observed in the focal plane along the sonication pattern, ensuring a homogenous ablation. The white dotted line represents the prescribed treatment plane.

Double linear sonication (Fig. 4) comprising 10 individual foci displaced on two parallel lines (4-mm gap between the
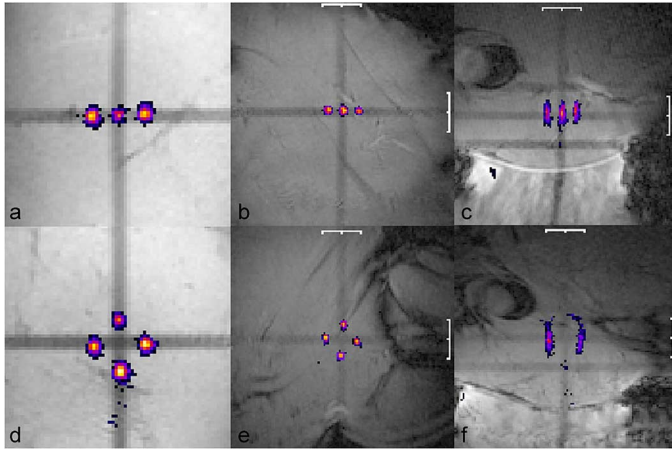
Fig. 2. Experimental correction of foci positioning for linear (a–c) and circular (d–f) patterns, for *in vivo* (b–c and e-f) and *ex vivo* experiments (a, d). Two orthogonal slices are presented for *in vivo* sonications (coronal slice: b and e; axial slice: c and f) with $\text{FOV} = 128 \times 128 \text{ mm}^2$, while zoom-in of the focal plane is illustrated for the *ex vivo* pilot sonication (a and d) with shown $\text{FOV} = 64 \times 64 \text{ mm}^2$.
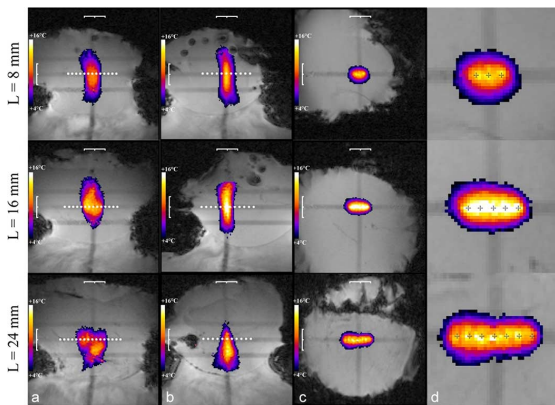

Fig. 3. *Ex vivo* temperature maps shown in three orthogonal planes (a: axial, b: sagittal, and c: coronal) for MRgHIFU single linear sonication pattern ($L = 8$, $L = 16$, and $L = 24$ mm) at the end point of the ablative sonication (voxel size: $1 \times 1 \times 5 \text{ mm}^3$ and FOV: $128 \times 128 \text{ mm}^2$). White line represents the prescribed treatment plane after experimental correction of foci positioning (as shown in Fig. 2). d: Closer view of the described volumetric pattern, illustrating the resulting temperature build-up in the coronal plane (zoom-in $\times$ 3). Please also note the sonicated points, illustrated by "+" markers.

lines) was also successfully performed. Each individual focus was clearly visible at the beginning of the sonication ($t_1 = 12 \text{ s}$) in the coronal slice [Fig. 4(a)], while at a later stage ($t_2 = 40 \text{ s}$), the temperature elevation became homogenous in the entire sonicated volume [see Fig. 4(b)] due to the diffusion process. Acoustic energies delivered per target focus, as recorded by the SW interface, are also presented in Fig. 4(c). The edge foci received significantly more energy while undergoing a similar temperature regime as the central foci. Linear scan sonication in *ex vivo* heterogenous tissues [shown in Fig. 4(d)] demonstrated the performance of the temperature controller under more challenging conditions. Two foci were located within the muscle (F1 and F2), one focus (F3) at the interface kidney/muscle, another one (F4) in the renal cortex and the last one (F5) in the renal medulla. The thermal history was

similar for the five sonicated foci, see Fig. 4(e) and (f) and their mean temperature elevation in steady-state regime was 18.1 °C (± 0.6 °C SD) versus 17.5 °C prescribed value. Note, the pilot sonication [see the inset in Fig. 4(e)] permitted to estimate the relative difference of focal point heating efficacy along the sonication pattern. Here, a ratio of 2.7 was determined between the Turkey pectoral muscle and the bovine kidney.

Fig. 5(a)–(c) provides more detailed insights of the temperature evolution in three orthogonal planes during MRgHIFU sonication of a 4 mm $\times$ 16 mm double linear sonication pattern at different moments. During the steady-state regime, the flat-top temperature was constant ($\pm$ noise), but the edges of the thermal build-up were expanding and smoothing because of the diffusion process (hence, the interest in fast treatment with a rapidly convergent controller). The surface representation (evolution with time) of a 1-D temperature profile is illustrated in Fig. 5(d) and (e).

The performance of the automatic controller was also demonstrated for circular scan trajectories of different sizes. Fig. 6 presents the temperature maps of the axial (a), sagittal (b), and coronal (c and d) planes, at the end of the MRgHIFU sonication process along circular trajectories with three different diameters ($D = 8$, $D = 16$, and $D = 24$ mm). Note the white dotted line representing the prescribed treatment plane. A drift of the thermal build-up of 3–12 mm towards the transducer was measured; this value increased linearly with the circular pattern's diameter. For the largest circular pattern (24 mm diameter), the available power of the HIFU device was insufficient to ensure the homogenization of the temperature profile along the sonication pattern, i.e., it is a hardware limitation of the system.

B. In Vivo Experimental Demonstration of the Temperature Controller

Examples of line scan ($L = 16$ mm) and circular scan ($D = 16$ mm) ablations are shown in Fig. 7 and Fig. 8, respectively, at the end point of the sonication. Temperature maps in two orthogonal planes are represented in frames a and b (axial and coronal, respectively, for both figures), while the temperature elevation in selected foci (three foci for linear trajectories and four foci for circular trajectories) is illustrated in frame c. The chosen foci in this figure actually correspond to the pilot sonication locations. Temperature versus time curves indicated a similar thermal history from one focus to another, regardless of the sonication pattern. The prescribed temperature elevation of 16 °C was reached rapidly for linear trajectories.

The thermal drift towards the near field for the circular scan, yielding a pre-focal large hot-spot, is evidenced by the thermal history of one pixel situated 12 mm below the focus in the axial plane [Fig. 8(d)]. There, the maximum temperature (20 °C) is significantly higher than in the focal plane itself (16 °C).

The temperature profile along the HIFU beam direction is represented in Fig. 7(d) and Fig. 8(e). Again, a general tendency of the maximum temperature elevation to drift towards the near field of the transducer for the circular scan is observed [Fig. 8(e)]. Regarding the linear trajectory, the thermal build-up remained longitudinally symmetrical with respect to the prescribed position of focal plane. Note, before each volumetric
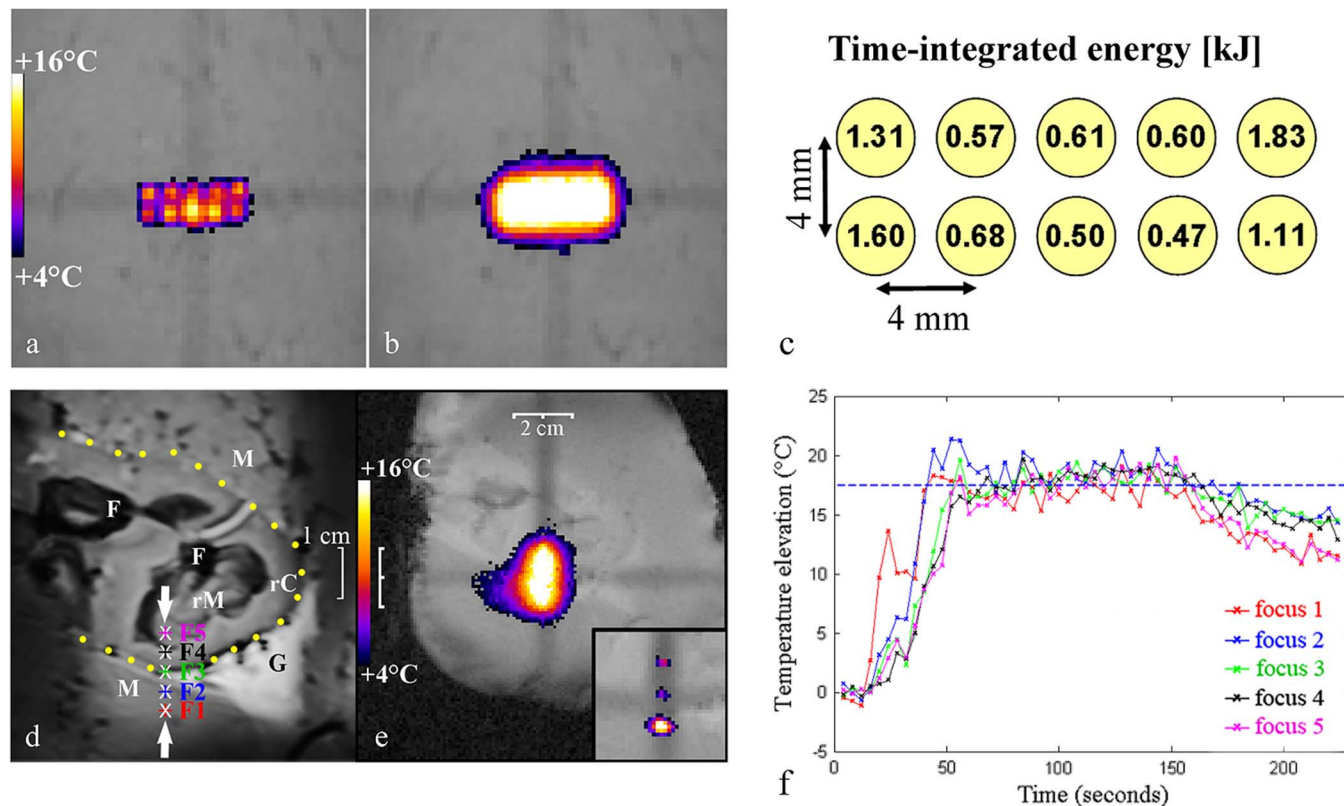
Fig. 4. a–c: Illustration of double linear scan volumetric ablation in *ex vivo* muscle: 10 individual foci displaced on two parallel lines were sonicated in this experiment. Every point is independently visible at the early stage of the sonication (a: coronal slice) at $t_1 = 12$ s and a uniform thermal build up region is visible (b: coronal slice) at a later stage $t_2 = 40$ s. Temperature elevation color code is from $+4\,°C$ to $+16\,°C$ and the shown FOV is 64×64 mm^2. c: Time-integrated acoustic energy delivered per target focus for the same experiment, as recorded by the SW interface. The edge foci received significantly more energy while undergoing a similar temperature regime as the central foci. d–f: *Ex vivo* linear scan sonication ($L = 16$ mm) in an heterogenous *ex vivo* sample. Distance scales are embedded. Anatomical structures (M: muscle, rC: renal cortex, rM: renal medulla, F: intra-renal fat, and G: standard ultrasonic gel for acoustic coupling) are visualized in the frame d) (coronal plane perpendicular to the direction of HIFU beam propagation) with high resolution, heavily $T2^*$ weighted FLASH-GRE. The position of the five sonicated foci (F1 to F5) is overlaid. e: Temperature elevation in the coronal plane at the end-point of the temperature-controlled sonication, together with the result of the pilot sonication required for the correction of the foci positions (see the inset at the lower right corner). f: Plot of temperature elevations for the sonicated foci (as measured in the coronal plane) versus time.

sonication, the focal plane was checked with the pilot sonication (Fig. 2) to avoid false interpretations of the asymmetrical temperature build-up.

Table III summarizes the thermal and dosimetric data obtained for the *in vivo* sonications (nine linear scans and seven circular scans, $L = D = 16$ mm). Temperature elevation (calculated as the average between all the sonicated foci) for line-scan sonications reached the prescribed temperature elevation (Θ_{top}) after a maximum 17 dynamics, while for the circular patterns, the prescribed temperature was reached later (three experiments) or not reached during the assigned treatment time (five experiments). In the latter cases, the controller used the first branch of (13), during the entire active period of sonication. This situation is equivalent to an asymptotical approach to a flat-top temperature elevation, which is lower than the prescribed value (Θ_{top}), but is the maximum reachable with the available acoustic power. In the end, this means that the temperature controller converges to a different steady state than prescribed, albeit in a stable manner. *In vivo* results of 11 experiments when steady-state was reached, indicated a similar

thermal history of each sonicated focus along the prescribed pattern, that was $17.3 \pm 0.5\,°C$ as compared to $16\,°C$ prescribed temperature elevation.

Please note that for the same linear sonication pattern, in two different experiments (ID 2 and 9), a factor of approximately two in energy was delivered in order to reach the same temperature elevation. Dosimetric data indicated a lower acoustic energy required by the controller for the linear pattern sonications (62.3 kJ, $\pm 33.7\%$) while higher energy (116.6 kJ, $\pm 10.9\%$) was necessary for the circular patterns for the same duration (120 s). Moreover, the calculated volume of the ablated region (240CEM@43 according to [25]) was 3.80 cc ($\pm 30\%$) for the linear scan and 17.8 cc ($\pm 11.4\%$) for the circular scan (considering also the thermal drift effect), indicating a volume to energy ratio of 0.061 and 0.153 cc/kJ, respectively. In addition, the near field to focal plane thermal contrast (NF-TC) calculated as the temperature elevation ratio between a location 12 mm below the focal plane on the symmetry axis of the transducer and the average temperature elevation along the foci pattern was found to be 0.86 for linear patterns and 1.33 for circular patterns.
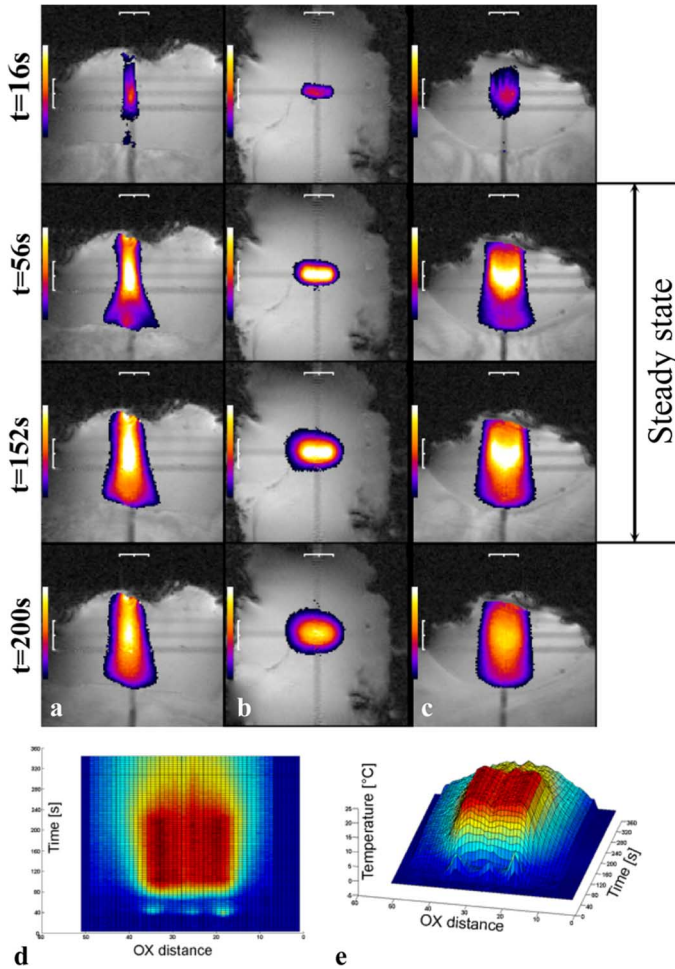
Fig. 5. Detailed insights on the temperature controller for the 16-mm double line sonication: axial (a), coronal (b), and sagittal (c) MR slices are shown in different HIFU sonication stages, FOV is 128×128 mm^2 each. Temperature elevation color code is from $+4\,^\circ$C to $+16\,^\circ$C. The corresponding time point is indicated on the left. During the steady-state regime, the maximum (central) temperature is constant ($\pm$ noise), but the edges of the thermal build-up are expanding and smoothing because of the diffusion process (hence, the interest in fast treatment with a rapidly convergent controller). (d), (e): Evolution with time of the 1-D central temperature profile (flat and surface representation).
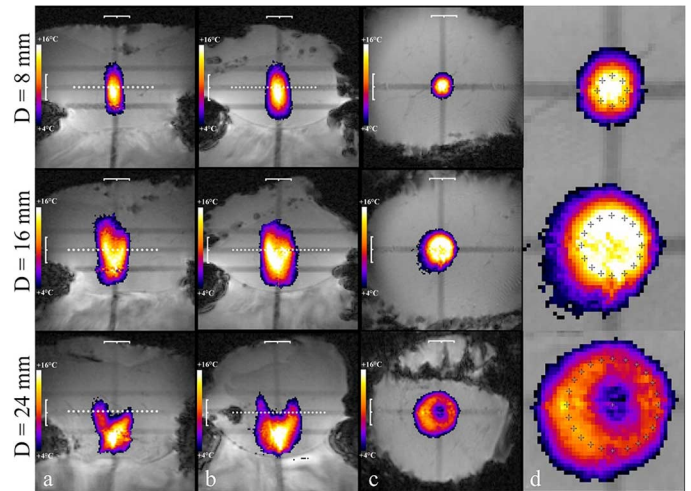

Fig. 6. *Ex vivo* temperature maps overlaid on magnitude images for three orthogonal planes (a: axial, b: sagittal, and c: coronal) for MRgHIFU circular sonication patterns ($D = 8$, $D = 16$, and $D = 24$ mm), under active control at the end of sonication (voxel size: $1 \times 1 \times 5$ mm^3 and FOV: 128×128 mm^2). Temperature elevation color code is from $+4\,^\circ$C to $+16\,^\circ$C. White line represents the prescribed treatment plane after the experimental correction of foci positioning (as shown in Fig. 2). d: Closer view of the described volumetric pattern, in the coronal plane, illustrating the homogenous temperature build-up (zoom-in $\times 3$). Please also note the sonicated points illustrated by "+" markers.

IV. DISCUSSION

When sonicating large volumes of tissue using multiple HIFU foci disposed on different trajectory patterns, automatic feedback control is desirable to avoid overtreatment in some areas and undertreatment in others. A sharp delineation of the ablated tissue, homogenous ablation, and increased treatment efficiency are also required. In order to meet all these criteria, a new automatic temperature controller using nonlinear negative reaction is presented, and evaluated for different volumetric trajectories. The present controller is based on a generic ("universal") algorithm and thus, no tissue specific tuning parameter is necessary. This feature simplifies the overall workflow of the treatment procedure because it does not need to estimate/identify the parameters preliminarily. This way, each controlled pixel receives a guaranteed thermal dose due to the automatic feedback. Accurate temperature control was demonstrated to be feasible both *ex vivo* and *in vivo* during fast volumetric ablation.

Electronic steering is advantageous for rapid volumetric ablation, but it produces focal intensity reduction and an alteration of the focal spot shape. A major advantage of this controller is that there is no need for explicit information on the acoustic field pattern.

Due to the diffusion's preferential border cooling and the electronic steering, higher energies must be applied at the extremities of the line-scan trajectory [see Fig. 4(c)]. The controller automatically adjusts the delivered energy per focus to compensate these effects.

The feedback loop here was rapidly converging (in typically three sampling points for the new controller, compared with typically 8–10 sampling points for the older PID controller) in agreement with the numerical simulations (see Table I). For line scan sonications [see Fig. 7(c)], the steady-state regime was attained typically within duration of less than 1 minute, and 16 s in the best case. For circle sonication patterns, the steady-state regime was attained later, or could not be attained during the assigned treatment duration, due to the higher peripheral heat flow and the hardware limitations of the device. The mean value for volume/energy ratio indicated higher dose efficiency of the circular scan versus the linear scan by approximately a factor of 2.5.

As the actual controller is nonparametric, the question of tuning parameter errors is not applicable. Overall, with the absence of an explicitly predefined temperature slope, the principle of spatial uniformization of temperature over the foci and nonparametric feature were empirically sufficient conditions to achieve stable controller performance in all experimental studies performed with this method. The target elevation of temperature should not be reached in less than two sampling points, to enable the applicability of (14).
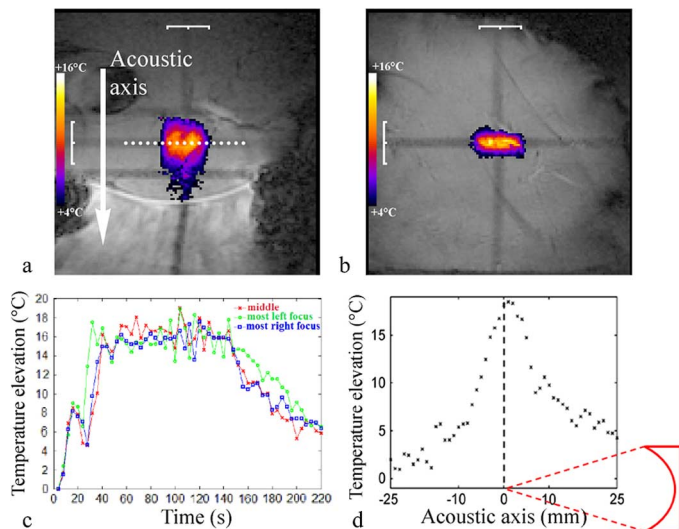
Fig. 7. *In vivo* temperature maps in axial (a) and coronal (b) planes (FOV = 128×128 mm^2) at the end point of a linear ablative sonication (L = 16 mm, 120 s duration, corresponding to sample 2 of Table III). Temperature elevation color code is from $+4\,°$C to $+16\,°$C. The acoustic axis points towards the transducer, corresponding to positive numbers for pre-focal thermal drift. The temperature elevation in three chosen foci, measured in the coronal plane (at the extremities and center of the linear scan pattern), are presented in frame c. The transient temperature elevation at the beginning of the sonication (maximum elevation reached at t = 18 s) corresponds to the pilot test shot for foci alignment [see Fig. 2(b) and (c)]. Images (d) illustrates the 1-D temperature profile along the beam propagation axis. The zero coordinate stands for the prescribed treatment plane.

Fig. 8. *In vivo* temperature maps in axial (a) and coronal (b) planes (FOV = 128×128 mm^2) at the end ($\Delta t = 120$ s) of a circular sonication pattern (D = 16 mm, corresponding to sample 11 of Table III). Temperature elevation color code is from $+4\,°$C to $+16\,°$C. The acoustic axis points towards the transducer, corresponding to positive numbers for pre-focal thermal drift. The temperature elevation in four chosen foci, measured in the coronal plane (one chosen per quadrant sector: up, down, right, and left), are shown in frame c, while the temperature elevation in one pixel situated 12 mm bellow the focus (axial plane) is shown in frame d. The transient temperature elevation at the beginning of the sonication (maximum elevation reached at t = 18 s, frame c) corresponds to the pilot test shot for foci alignment [see Fig. 2(e) and (f)]. Frame e illustrates the 1-D temperature profile along the beam propagation axis. The zero coordinate stands for the prescribed treatment plane. There is a 13-mm shift of the thermal build-up towards the transducer.

When applying the P²ID controller to the experimental conditions, three limitations were identified: uncompensated motion conditions, pre-focal thermal build-up accumulation with the circular scan, and hardware capabilities to deliver sufficient acoustic energy to reach the predefined target level of temperature. In contrast to the parametric PID controller [17], here the Laplacian operator of temperature is not calculated; therefore, noise-robustness is expected to be significantly improved.

Heterogenous *ex vivo* tissues have been used in this experimental study as challenging test condition for the P2ID controller that has accurately compensated for a large spatial variation of heating absorption rate, a factor of 2.7 here. Further testing under multiple conditions including spurious temperature artifacts, lower SNR, highly perfused organs or with other device geometries (i.e., intracavitary heating) should be prospectively addressed.

An important observation made for volumetric HIFU sonications using circular scans concerned the longitudinally asymmetric temperature profile, indicating a significant thermal drift towards the near field. These effects were found to be dependent on the size of the trajectory and on the ultrasound attenuation coefficient. Although not investigated here, the frequency of the ultrasound would also play a role, because a higher frequency would increase the attenuation coefficient. The thermal drift towards the near field was observed both *ex vivo* and *in vivo*, for all circular trajectories with different diameters, and was determined to be approximately equal to the circle diameter (aperture number F/D ~ 1). For line-scan sonication, the temperature elevation remained longitudinally symmetrical with respect to the
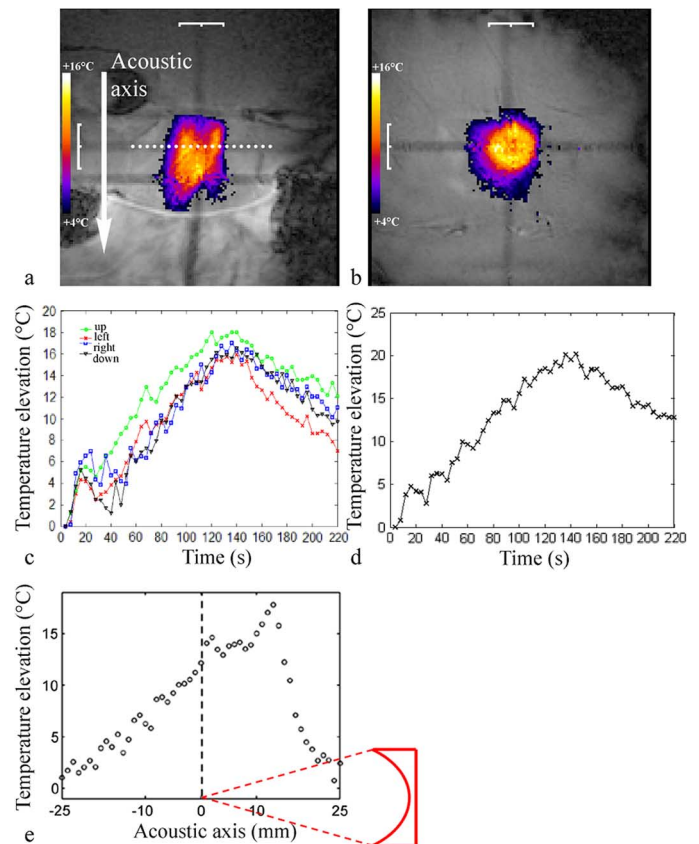
prescribed position of focal plane. Nevertheless, alteration of the thermal build up homogeneity in the axial plane occurred for the largest linear pattern (24 mm); this effect being probably related to the alteration of focusing quality far from the transducer's symmetry axis. As a general observation of the experimental study using rapid volumetric HIFU ablation under continuous sonication, it appears that the 2D circular scans tested have a higher volumetric ablation rate than the linear scans, at the expense of significantly enhanced heating in the pre-focal region. Meanwhile, line-scan sonications appeared to provide the best results for volumetric treatments with drift-free and uniform thermal build-up. These effects are to be considered when designing a sonication geometry with respect to uniformity, heating time, volumetric rate of ablation, and power requirements. The benefits of a particular geometry also depend on the clinical target in terms of its histopathology and anatomic environment.

The topology of the near-field thermal build-up depends on the sonication pattern, aperture number, and sparsity of the

TABLE III
THERMAL AND DOSIMETRIC DATA FOR THE *in vivo* EXPERIMENTS
(L = D = 16 mm, TARGET TEMPERATURE ELEVATION 16 °C)

Line - 16 mm

ID	Duration of transient regime before steady state (s)	Mean foci temperature elevation in steady-state regime (°C)	SDT in steady-state regime (°C)	Energy (kJ)	NF-TC***
#1	32	17.3	1.32	65.5	1.2
#2	20	17.6	1.13	41.3	0.5
#3	44	17.6	1.99	60.5	1.1
#4	68	17.5	1.86	79.5	0.9
#5	16	17.7	1.89	60.1	1.1
#6	16	18.1	2.06	43.6	1
#7	44	16.6	1.66	70.4	0.7
#8	32	16.3	1.26	65.4	0.5
#9	60	17.0	1.05	74.7	0.8

Circle - 16 mm

ID	Duration of transient regime before steady state (s)	Mean foci temperature elevation during last 10 dyn (°C)	SDT in last 10 dyn (°C)	Energy (kJ)	NF-TC***
#10	not reached	13.5**	1.52**	108.3	1.4
#11	96	17.0	0.95	107.1	1.3
#12	not reached	14.8**	0.95**	107.7	1.4
#13	not reached	NA*	NA*	NA*	
#14	not reached	12.9**	1.69**	124.3	1.2
#15	not reached	12.0**	1.31**	129.4	1.3
#16	100	16.8	2.26	123.1	1.4

NA—not available owing to missing data

** temperature or STD average was calculated for the last 10 dynamics before the end point of the ablative sonication

*** near field to focal plane thermal contrast (NF-TC)

phased-array transducer and the field is almost linear in this region [26]. When shocks form within the region of the main focus, nonlinear waveform distortion is almost negligible in the pre-focal regions of lower amplitude [26]. Therefore, scaling the emitted acoustic power does not change significantly the intrinsic topology of the acoustic intensity in the near field. Nevertheless, the occurrence of shock waves can increase the thermal contrast between the focal and pre-focal regions, owing to the nonlinear absorption at the focus. Reciprocally, for a given temperature elevation at the focus, near-field heating may be decreased. The potential impact of shock waves in the acoustic regime on the temperature controller's performance has not been investigated here because the initial intensity at the transducer surface was one order of magnitude less than that theoretically required [26] to enter that regime.

At the interaction of the HIFU beam (which is a propagating wave) with the soft tissue/air interface (e.g., skin, air-filled bowel) or soft tissue/bone interface, various thermo-acoustical side effects can occur when using the volumetric sonication paradigm [27]. These phenomena may limit the clinical applicability of volumetric ablation, despite the dosimetric advantage.

Movement hampers the MRgHIFU procedures for three known reasons: loss of treatment efficiency by spatial spreading of the delivered energy, risk of unintended lesions caused by overheating of adjacent healthy tissue, and artifacts in the MR monitoring [28]. Automatic temperature control is not intended to primarily address these issues, which should be corrected using dedicated methods, e.g., see [29] and [30]. The automatic control method described here is compatible with any motion compensation method if its time latency is sufficiently low. This means that the input function of the controller should be a motion-compensated temperature map, and the sonication pattern should consist of motion-compensated geometric coordinates of the foci. We can anticipate the following behavior of the controller in the case of single event accidental motion: the initially heated tissue will be shifted outside the prescribed pattern of foci in the transducer coordinates system and therefore, the controlled state function (focal point wise temperature) will drop sharply. The controller will react to this event by increasing the applied energy until the state function converges back to the prescribed target value according to the time derivative of (5).

V. CONCLUSION

In this paper, we described a new temperature controller for therapeutic ultrasound, which does not require tuning parameters. We also presented *ex vivo* and *in vivo* validation using MRgHIFU for different volumetric sonication patterns, demonstrating accurate control of the temperature in all foci along the sonication pattern. The strength of convergence of the controller was sufficient for good performance without requiring *a priori* knowledge of the thermoacoustic parameters of tissue. The spatio-temporal control of the temperature in the focal plane enabled meaningful comparison of different sonication patterns in terms of dosimetry and near-field safety. Further standardization of the therapeutic procedure may be required for clinical treatments using volumetric HIFU.

APPENDIX
EXPERIMENTAL CORRECTION OF THE GEOMETRICAL ABERRATION OF THE FOCI POSITIONS USING A PILOT SONICATION

Case 1. Line Scan Sonication: The pilot sonication consisted of three interleaved foci, of which two were executed at the extremities of the linear pattern and one was executed at its center. The coordinates of the theoretical foci positions are denoted as $(x_1, 0)$, $(x_2, 0)$, and $(x_3, 0)$. The local geometric errors of the actual foci positions, as determined from the MR thermometry data at the end of the pilot sonication, are denoted as $\delta x_i, \delta y_i$ with $i = 1,2,3$ [see Fig. 9(a)]. The parabolic approximation of the geometric error (or the equivalent local distortion vector) of the focus position relative to its theoretical (or prescribed) position is given as a function of the theoretical position (x) along the linear pattern as follows:

$$\delta x(x) = \delta x_1 \cdot \frac{(x-x_2)\cdot(x-x_3)}{(x_1-x_2)\cdot(x_1-x_3)} + \delta x_2 \cdot \frac{(x-x_1)\cdot(x-x_3)}{(x_2-x_1)\cdot(x_2-x_3)} + \delta x_3 \cdot \frac{(x-x_1)\cdot(x-x_2)}{(x_3-x_1)\cdot(x_3-x_2)} \quad \text{(A1)}$$

$$\delta y(x) = \delta y_1 \cdot \frac{(x-x_2)\cdot(x-x_3)}{(x_1-x_2)\cdot(x_1-x_3)} + \delta y_2 \cdot \frac{(x-x_1)\cdot(x-x_3)}{(x_2-x_1)\cdot(x_2-x_3)} + \delta y_3 \cdot \frac{(x-x_1)\cdot(x-x_2)}{(x_3-x_1)\cdot(x_3-x_2)}. \quad \text{(A2)}$$
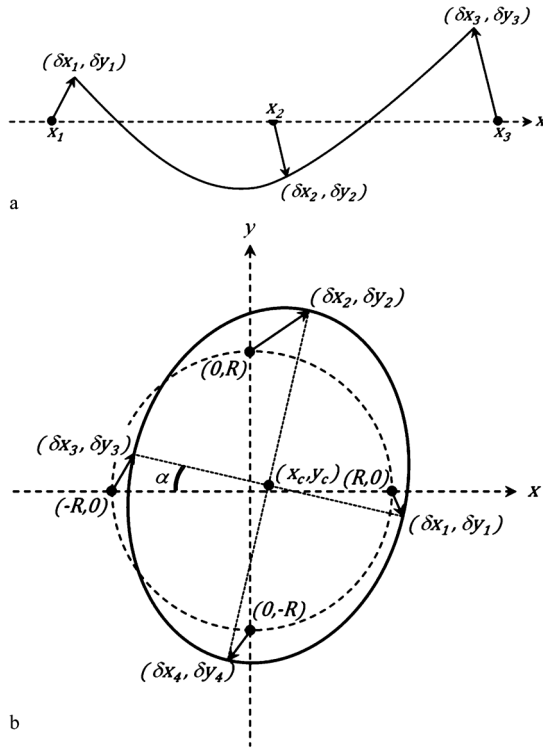
Fig. 9. Theoretical foci positions and the local geometric errors of the foci positions (as determined from the MR thermometry data) for linear (a) and circular (b) pilot sonication.

During the ablative sonication, performed under automatic control of temperature, each prescribed position of a focus within the linear pattern was pre-shifted from its theoretical position by quantities equal to the opposite distortion vector according to

$$
\begin{cases}
x'(x) = x - \delta x(x) \\
y'(x) = y - \delta y(x)
\end{cases}. \tag{A3}
$$

This correction re-established a regular linear pattern of foci as a second-order compensation.

Case 2. Circular Scan Sonication: The pilot sonication consisted of four interleaved foci, symmetrically executed one per quadrant, at the theoretical positions of $(R, 0)$, $(0, R)$, $(-R, 0)$, and $(1, -R)$. The local geometric errors of the actual foci positions, as determined from the MR thermometry data at the end of the pilot sonication, are denoted as $\delta x_i, \delta y_i$ with $i = 1,2,3$ [see Fig. 9(b)]. Under the hypothesis that the modulus of the local distortion vector is much smaller than the circle's radius R, the first order perturbation of the circle into an ellipse can be approximated by the following five parameters representing the ellipse's center coordinates (x_c, y_c), semi-axes (a, b), and rotation angle (α)

$$
x_c \cong \frac{1}{4} \cdot (\delta x_1 + \delta x_2 + \delta x_3 + \delta x_4) \tag{A4}
$$

$$
y_c \cong \frac{1}{4} \cdot (\delta y_1 + \delta y_2 + \delta y_3 + \delta y_4) \tag{A5}
$$

$$
a \cong R + \frac{\delta x_1 - \delta x_3}{2} \tag{A6}
$$

$$
b \cong R + \frac{\delta y_2 - \delta y_4}{2} \tag{A7}
$$

$$
\alpha \cong \frac{1}{2} \cdot \left[atan\left(\frac{\delta x_4 - \delta x_2}{2b} \right) + atan\left(\frac{\delta y_1 - \delta y_3}{2a} \right) \right]. \tag{A8}
$$

During the ablative sonication, performed under automatic control of temperature, each prescribed position of a focus within the circular pattern was pre-shifted from its theoretical position $(R \cdot \cos\theta, R \sin\theta)$ as a function of the polar angle on that circle (θ) according to

$$
\begin{cases}
x'(\theta) = -x_c + \frac{R \cdot \cos(\theta - \alpha)}{a} \\
y'(\theta) = -y_c + \frac{R \cdot \sin(\theta - \alpha)}{b}
\end{cases}. \tag{A9}
$$

This correction reestablished a regular circular pattern of foci as a first order approximation compensating for the average spatial shift, the Ox and Oy axes compression or expansion, and for the angular rotation of the local acoustic frame of reference versus the MRI frame.

REFERENCES

[1] S. Terraz, A. Cernicanu, M. Lepetit-Coiffé, M. Viallon, R. Salomir, G. Mentha, and C. D. Becker, "Radiofrequency ablation of small liver malignancies under magnetic resonance guidance: Progress in targeting and preliminary observations with temperature monitoring," *Eur. Radiol.*, vol. 20, no. 4, pp. 886–897, Apr. 2010.

[2] K. Hynynen, O. Pomeroy, D. N. Smith, P. E. Huber, N. J. McDannold, J. Kettenbach, J. Baum, S. Singer, and F. A. Jolesz, "MR imaging-guided focused ultrasound surgery of fibroadenomas in the breast: A feasibility study," *Radiology*, vol. 219, no. 1, pp. 176–185, Apr. 2001.

[3] E. A. Stewart, W. M. Gedroyc, C. M. Tempany, B. J. Quade, Y. Inbar, T. Ehrenstein, A. Shushan, J. T. Hindley, R. D. Goldin, M. David, M. Sklair, and J. Rabinovici, "Focused ultrasound treatment of uterine fibroid tumors: Safety and feasibility of a noninvasive thermoablative technique," *Am. J. Obstet. Gynecol.*, vol. 189, no. 1, pp. 48–54, Jul. 2003.

[4] C. M. Tempany, E. A. Stewart, N. McDannold, B. J. Quade, F. A. Jolesz, and K. Hynynen, "MR imaging-guided focused ultrasound surgery of uterine leiomyomas: A feasibility study," *Radiology*, vol. 226, no. 3, pp. 897–905, Mar. 2003.

[5] R. Salomir, J. Palussière, F. C. Vimeux, J. A. de Zwart, B. Quesson, M. Gauchet, P. Lelong, J. Pergrale, N. Grenier, and C. T. Moonen, "Local hyperthermia with MR-guided focused ultrasound: Spiral trajectory of the focal point optimized for temperature uniformity in the target region," *J. Magn. Reson. Imag.*, vol. 12, no. 4, pp. 571–583, Oct. 2000.

[6] J. Palussière, R. Salomir, B. Le Bail, R. Fawaz, B. Quesson, N. Grenier, and C. T. Moonen, "Feasibility of MR-guided focused ultrasound with real-time temperature mapping and continuous sonication for ablation of VX2 carcinoma in rabbit thigh," *Magn. Reson. Med.*, vol. 49, no. 1, pp. 89–98, Jan. 2003.

[7] M. O. Köhler, C. Mougenot, B. Quesson, J. Enholm, B. Le Bail, C. Laurent, C. T. Moonen, and G. J. Ehnholm, "Volumetric HIFU ablation under 3D guidance of rapid MRI thermometry," *Med. Phys.*, vol. 36, no. 8, pp. 3521–3535, Aug. 2009.

[8] M. J. Voogt, H. Trillaud, Y. S. Kim, W. P. Mali, J. Barkhausen, L. W. Bartels, R. Deckers, N. Frulio, H. Rhim, H. K. Lim, T. Eckey, H. J. Nieminen, C. Mougenot, B. Keserci, J. Soini, T. Vaara, M. O. Köhler, S. Sokka, and M. A. van den Bosch, "Volumetric feedback ablation of uterine fibroids using magnetic resonance-guided high intensity focused ultrasound therapy," *Eur. Radiol.*, vol. 22, no. 2, pp. 411–417, Feb. 2012.

[9] F. A. Jolesz and N. McDannold, "Current status and future potential of MRI-guided focused ultrasound surgery," *J. Magn. Reson. Imag.*, vol. 27, no. 2, pp. 391–399, Feb. 2008.

[10] R. Salomir, A. S. Delemazure, J. Palussière, O. Rouvière, F. Cotton, and J. Y. Chapelon, "Image-based control of the magnetic resonance imaging-guided focused ultrasound thermotherapy," *Top. Magn. Reson. Imag.*, vol. 17, no. 3, pp. 139–151, Jun. 2006.

[11] Y. Ishihara, A. Calderon, H. Watanabe, K. Okamoto, Y. Suzuki, K. Kuroda, and Y. Suzuki, "A precise and fast temperature mapping using water proton chemical shift," *Magn. Reson. Med.*, vol. 34, no. 6, pp. 814–823, Dec. 1995.

[12] H. Rempp, P. Martirosian, A. Boss, S. Clasen, A. Kickhefel, M. Kraiger, C. Schraml, C. Claussen, P. Pereira, and F. Schick, "MR temperature monitoring applying the proton resonance frequency method in liver and kidney at 0.2 and 1.5 T: Segment-specific attainable precision and breathing influence," *MAGMA*, vol. 21, no. 5, pp. 333–343, Sep. 2008.

[13] R. Salomir, M. Viallon, A. Kickhefel, J. Roland, D. Morel, L. Petrusca, V. Auboiroux, T. Goget, S. Terraz, C. D. Becker, and P. Gross, "Reference-free PRFS MR-thermometry using near-harmonic 2-D reconstruction of the background phase," *IEEE Trans. Med. Imag.*, vol. 31, no. 2, pp. 287–301, Feb. 2012.

[14] A. Vanne and K. Hynynen, "MRI feedback temperature control for focused ultrasound surgery," *Phys. Med. Biol.*, vol. 48, no. 1, pp. 31–43, Jan. 2003.

[15] N. McDannold, C. M. Tempany, F. M. Fennessy, M. J. So, F. J. Rybicki, E. A. Stewart, F. A. Jolesz, and K. Hynynen, "Uterine leiomyomas: MR imaging-based thermometry and thermal dosimetry during focused ultrasound thermal ablation," *Radiology*, vol. 240, no. 1, pp. 263–272, Jul. 2006.

[16] R. Salomir, M. Rata, D. Cadis, L. Petrusca, V. Auboiroux, and F. Cotton, "Endocavitary thermal therapy by MRI-guided phased-array contact ultrasound: Experimental and numerical studies on the multi-input single-output PID temperature controller's convergence and stability," *Med. Phys.*, vol. 36, no. 10, pp. 4726–4741, Oct. 2009.

[17] R. Salomir, F. C. Vimeux, J. A. de Zwart, N. Grenier, and C. T. Moonen, "Hyperthermia by MR-guided focused ultrasound: Accurate temperature control based on fast MRI and a physical model of local energy deposition and heat conduction," *Magn. Reson. Med.*, vol. 43, no. 3, pp. 342–347, Mar. 2000.

[18] C. Mougenot, R. Salomir, J. Palussière, N. Grenier, and C. T. Moonen, "Automatic spatial and temporal temperature control for MR-guided focused ultrasound using fast 3D MR thermometry and multispiral trajectory of the focal point," *Magn. Reson. Med.*, vol. 52, no. 5, pp. 1005–1015, Nov. 2004.

[19] C. Mougenot, B. Quesson, B. D. de Senneville, P. L. de Oliveira, S. Sprinkhuizen, J. Palussière, N. Grenier, and C. T. Moonen, "Three-dimensional spatial and temporal temperature control with MR thermometry-guided focused ultrasound (MRgHIFU)," *Magn. Reson. Med.*, vol. 61, no. 3, pp. 603–614, Mar. 2009.

[20] R. Chopra, N. Baker, V. Choy, A. Boyes, K. Tang, D. Bradwell, and M. J. Bronskill, "MRI-compatible transurethral ultrasound system for the treatment of localized prostate cancer using rotational control," *Med. Phys.*, vol. 35, no. 4, pp. 1346–1357, Apr. 2008.

[21] R. Chopra, J. Wachsmuth, M. Burtnyk, M. A. Haider, and M. J. Bronskill, "Analysis of factors important for transurethral ultrasound prostate heating using MR temperature feedback," *Phys. Med. Biol.*, vol. 51, pp. 827–844, Feb. 2006.

[22] E. Delabrousse, R. Salomir, A. Birer, C. Paquet, F. Mithieux, J. Y. Chapelon, F. Cotton, and C. Lafon, "Automatic temperature control for MR-guided interstitial ultrasound ablation in liver using a percutaneous applicator: *Ex vivo* and *in vivo* initial studies," *Magn. Reson. Med.*, vol. 63, no. 3, pp. 667–679, 2010.

[23] M. Rata, R. Salomir, R. Umathum, J. Jenne, C. Lafon, F. Cotton, and M. Bock, "Endoluminal ultrasound applicator with an integrated RF coil for high-resolution magnetic resonance imaging-guided high-intensity contact ultrasound thermotherapy," *Phys. Med. Biol.*, vol. 53, no. 22, pp. 6549–6567, Nov. 2008.

[24] R. D. Peters, R. S. Hinks, and R. M. Henkelman, "Heat-source orientation and geometry dependence in proton-resonance frequency shift magnetic resonance thermometry," *Magn. Reson. Med.*, vol. 41, no. 5, pp. 909–918, May 1999.

[25] S. A. Sapareto and W. C. Dewey, "Thermal dose determination in cancer therapy," *Int. J. Radiat. Oncol. Biol. Phys.*, vol. 10, no. 6, pp. 787–800, Jun. 1984.

[26] P. V. Yuldashev, S. M. Shmeleva, S. A. Ilyin, O. A. Sapozhnikov, L. R. Gavrilov, and V. A. Khokhlova, "The role of acoustic nonlinearity in tissue heating behind a rib cage using a high-intensity focused ultrasound phased array," *Phys. Med. Biol.*, vol. 58, no. 8, pp. 2537–2559, 2013.

[27] M. Viallon, L. Petrusca, V. Auboiroux, T. Goget, L. Baboi, C. D. Becker, and R. Salomir, "Experimental methods for improved spatial control of thermal lesions in magnetic resonance-guided focused ultrasound ablation," *Ultrasound Med. Biol.*, vol. 39, no. 9, pp. 1580–1595, 2013.

[28] M. Viallon, S. Terraz, J. Roland, E. Dumont, C. D. Becker, and R. Salomir, "Observation and correction of transient cavitation-induced PRFS thermometry artifacts during radiofrequency ablation, using simultaneous ultrasound/MR imaging," *Med. Phys.*, vol. 37, no. 4, pp. 1491–1506, 2010.

[29] V. Auboiroux, L. Petrusca, M. Viallon, T. Goget, C. D. Becker, and R. Salomir, "Ultrasonography-based 2D motion-compensated HIFU sonication integrated with reference-free MR temperature monitoring: A feasibility study *ex vivo*," *Phys. Med. Biol.*, vol. 57, no. 10, pp. N159–N171, 2012.

[30] Z. Celicanin, V. Auboiroux O. Bieri, L. Petrusca, F. Santini, M. Viallon, K. Scheffler, and R. Salomir, "Real-time method for motion-compensated MR thermometry and MRgHIFU treatment in abdominal organs," *Magn. Reson. Med.*, Nov. 2013.